Comparison of the Vertical Distributions of Cloud Properties from Idealized Extratropical Deep Convection Simulations Using Various Horizontal Resolutions

WEI HUANG

Shanghai Typhoon Institute, and Key Laboratory of Numerical Modeling for Tropical Cyclone of the China Meteorological Administration, Shanghai, China

J.-W. BAO

NOAA/Earth System Research Laboratory, Boulder, Colorado

XU ZHANG AND BAODE CHEN

Shanghai Typhoon Institute, and Key Laboratory of Numerical Modeling for Tropical Cyclone of the China Meteorological Administration, Shanghai, China

(Manuscript received 5 June 2017, in final form 15 January 2018)

ABSTRACT

The authors coarse-grained and analyzed the output from a large-eddy simulation (LES) of an idealized extratropical supercell storm using the Weather Research and Forecasting (WRF) Model with various horizontal resolutions (200 m, 400 m, 1 km, and 3 km). The coarse-grained physical properties of the simulated convection were compared with explicit WRF simulations of the same storm at the same resolution of coarse-graining. The differences between the explicit simulations and the coarse-grained LES output increased as the horizontal grid spacing in the explicit simulation coarsened. The vertical transport of the moist static energy and total hydrometeor mixing ratio in the explicit simulations converged to the LES solution at the 200-m grid spacing. Based on the analysis of the coarse-grained subgrid vertical flux of the moist static energy, the authors confirmed that the nondimensional subgrid vertical flux of the moist static energy varied with the subgrid fractional cloudiness according to a function of fractional cloudiness, regardless of the box size. The subgrid mass flux could not account for most of the total subgrid vertical flux of the moist static energy because the eddy-transport component associated with the internal structural inhomogeneity of convective clouds was of a comparable magnitude. This study highlights the ongoing challenge in developing scale-aware parameterizations of subgrid convection.

1. Introduction

The accuracy of numerical weather prediction (NWP) is highly dependent on parameterizations of unresolved subgrid physical processes. Subgrid convective parameterization at the so-called gray-zone horizontal resolutions (i.e., the grid spacing ~1–10 km) is a challenging problem in numerical weather prediction (Gerard 2007; Hong and Dudhia 2012). This is because the assumptions in traditional parameterizations of subgrid clouds, which are based on the concept of quasi equilibrium (QE) (Arakawa and Schubert 1974), are no longer applicable at these resolutions (see Plant and Craig 2008; Arakawa et al. 2011; Dorrestijn et al. 2013; Sakradzija et al. 2015 for more discussions).

Sakradzija et al. (2016) pointed out that according to previous studies (e.g., LeMone et al. 2010; Zhou et al. 2014; Ching et al. 2014), the characteristics of organized convective circulations simulated by a cloud resolving model at the gray-zone resolutions strongly depends on the horizontal grid size and the spatial scales of the simulated overturning at these resolutions tend to be greater than those in natural convection. Not using any parameterization of subgrid clouds at the gray-zone horizontal resolutions does not seem to alleviate the problem because it can cause errors in the simulation of convection initiation and precipitation rate (Bryan and Rotunno 2005; Roberts and Lean 2008). The problem

Corresponding author: Baode Chen, baode@typhoon.org.cn

DOI: 10.1175/MWR-D-17-0162.1

of parameterizing subgrid clouds at the gray-zone resolutions is also complicated by the fact that model-simulated dynamics at these resolutions behaves differently from that at horizontal resolutions much greater than 10 km, such that the model solution may falsely represent the effective subgrid convection in the form of resolved convective elements (Sakradzija et al. 2016).

Cloud resolved models (CRMs) and large-eddy simulation (LES) models are widely used as very effective tools for cloud process studies and for developing cloud parameterization suitable for the gray-zone resolutions because they can provide detailed information of cloud processes that cannot be observed (e.g., Khairoutdinov and Randall 2001; Bryan et al. 2003; Randall et al. 2003; Siebesma et al. 2003; Yano et al. 2005). Because of computational limitations, LES models have generally been used to simulate processes associated with shallow clouds in the atmospheric boundary layer (ABL), while CRMs are primarily used to simulate deep convection. Recently, LES models have started to be used in studies of deep convective processes. For example, Khairoutdinov et al. (2009) used an idealized LES with 100-m gridcell spacing to simulate tropical deep convection. McGee and van den Heever (2014) also used an LES model to investigate deep convection. This previous research provides encouraging results and motivates the need for additional LES studies of deep convection.

Deep convection in the tropics takes place largely under an environment of weak mean winds and is organized into distinct spatial patterns by interaction with large-scale motions and the constraint of underlying surface conditions. On the other hand, extratropical deep convection generally originates from external forcing, such as frontal systems or orography under strong mean winds, and is organized or regulated by certain dynamical conditions, such as vertical wind shear. It is usually characterized by rapid development, evident diurnal variation, and a short life cycle. Many studies have demonstrated that extratropical convective systems, such as supercell storms and squall lines, are generally poorly handled by convective parameterization schemes because of their distinct characteristics (e.g., Weisman et al. 2008). Therefore, it is imperative to evaluate and understand both the resolved and subgrid variabilities at different grid spacing for the purpose of improving subgrid convective parameterizations for convective weather simulation in the extratropics. To this end, an LES benchmark simulation of a 3D idealized supercell was carried out in this study to determine an appropriate grid spacing for explicitly simulating supercell storms without using a subgrid convective parameterization and to understand the subgrid cloud variability of different resolutions using LES coarse-graining datasets. A brief description of the model, experimental setup, and LES data analysis method is provided in section 2. Section 3 provides an overall description of the benchmark simulation and comparison of different resolution runs. Section 4 evaluates the subgrid cloud features of this convective system at different box sizes. Conclusions and a discussion are provided in section 5.

2. Model and LES data

a. Model setup

The Advanced Research core of the Weather Research and Forecasting (WRF) Model (WRF-ARW; Skamarock and Klemp 2008), version 3.7.1, was used in this study. The physics configuration includes the Thompson microphysics scheme (Thompson et al. 2004, 2008), which has five hydrometeor categories and predicts the number concentration of the rain and ice; the 1.5-order 3D prognostic TKE scheme (Klemp and Wilhelmson 1978) for subgrid mixing; and the surface layer scheme based on the Monin–Obukhov similarity theory. Radiative transfer was neglected for simplicity.

The model domain was 120 km × 120 km × 20 km along the x, y, and z directions, respectively. The model was initialized using the WRF idealized supercell initial condition, in which the temperature and humidity profiles are from Weisman and Klemp (1982) and represent an environment of moderate instability (Fig. 1). The environmental wind profile has unidirectional shear with the meridional wind set to zero, similar to the "straight" case of Weisman and Rotunno (2000). Because the purpose of this study was not related to the mechanism of the supercell itself, this simplification is acceptable. The convection was initiated by a thermal bubble with a horizontal radius of 10 km and a vertical radius of 1.5 km, with a potential temperature perturbation ranging from a maximum of 3 K at the center of the bubble (located at $x = 40$, $y = 60$, and $z = 1.5$ km) to zero at the edge of the bubble. Because the Coriolis effect is minimal over a short time period, the Coriolis parameter was also set to zero, as in Weisman and Rotunno (2000). The LES run used as a benchmark simulation (hereafter, B100) had a horizontal grid cell spacing of 100 m and a vertical spacing of approximately 100 m (200 levels). The time step was 0.3 s, and the experiment was run for 2.5 h. In addition, to evaluate the sensitivity of the results to the horizontal resolutions of the model, a series of experiments were conducted with different horizontal grid spacing (200 m, 400 m, 1 km, and 3 km; see Table 1) but with the same initial fields, model domain, vertical levels, time step, and physical configurations.

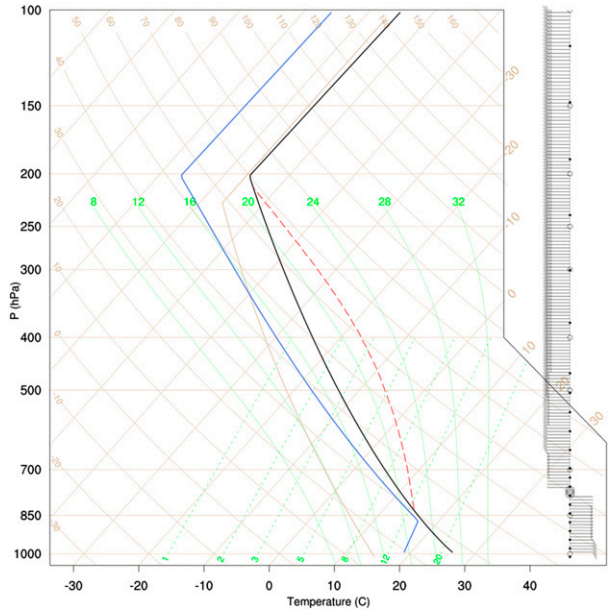

FIG. 1. Initial skew *T*–log*p* diagram showing temperature (black line), dewpoint temperature (blue line), a moist adiabat beginning at the level of free convection (red dashed line), and wind speed (barbs).

b. *Analysis procedure*

Using the 100-m benchmark simulation as the "true" solution, we constructed reference data for the different box sizes to evaluate the subgrid cloud characteristics at those scales. We chose the coarse-graining approach that was widely applied in previous studies (e.g., Honnert et al. 2011; Dorrestijn et al. 2013; Sakradzija et al. 2016). First, the LES model domain was divided into subdomains with specified box size Δ (200 m, 400 m, 1 km, and 3 km) for coarse-graining. The number of subdomains was, therefore, 600×600, 300×300, 120×120, and 40×40, respectively. In each subdomain, the mean variables at each model level were constructed by applying a box average to the LES output, as in Shin and Hong (2013). For any variable φ (including vertical velocity w), its mean and perturbation in a subdomain are defined as

$$\overline{\varphi} = \frac{1}{N}\sum \varphi_n \tag{1}$$

and

$$\varphi'_n = \varphi_n - \overline{\varphi}. \tag{2}$$

Here, the overbar and prime refer to the average and subgrid perturbation over the subdomain, respectively; N is the number of LES grid cells in each subdomain (e.g., for the box size of 3 km, $N = 30 \times 30 = 900$). For any subdomain, one can calculate the vertical flux of φ per unit density as

TABLE 1. Summary of the numerical experiments used in the study.

Experiment	Grid points	Horizontal grid size (m)
B100	$1200 \times 1200 \times 200$	100 (benchmark)
E200	$600 \times 600 \times 200$	200
E400	$300 \times 300 \times 200$	400
E1000	$120 \times 120 \times 200$	1000
E3000	$40 \times 40 \times 200$	3000

$$\overline{w\varphi} = \frac{1}{N}\sum w_n \varphi_n \tag{3}$$

and

$$\overline{w'\varphi'} = \frac{1}{N}\sum w'_n \varphi'_n. \tag{4}$$

Equations (3) and (4) are the total vertical transport and subgrid transport of φ, respectively. Using angle brackets to denote the domain average over all subdomains, the total and subgrid vertical transport of φ per unit density over the whole domain can be expressed as

$$<\overline{w\varphi}> = \frac{1}{M}\sum_m \overline{w\varphi} \tag{5}$$

and

$$<w'\varphi'> = \frac{1}{M}\sum_m \overline{w'\varphi'}, \tag{6}$$

where M is the number of subdomains (e.g., for the box size of 3 km, $M = 40 \times 40 = 1600$). Here, $M \times N$ is the total LES grid cells. To evaluate the subgrid cloud effect, this study focused on the vertical transport of moist static energy ($h = c_pT + Lq_v + gz$) and water vapor q_v following Arakawa and Wu (2013; hereafter, AW13), where T and q_v are the temperature and water vapor mixing ratio, respectively; c_p is the specific heat at constant pressure; L is the latent heat of evaporation; and gz is geopotential energy. In addition, the vertical transport of the total amount of hydrometeors (q_l) was also analyzed.

The subgrid cloudiness fraction σ, which is defined as the fractional area covered by convective updrafts in a coarse-graining subdomain, is a key parameter used in AW13 to develop a scale-aware parameterization. In this study, an LES grid cell was defined as cloudy when both the cloud hydrometeor concentration q_c was greater than 0.001 g kg^{-1} and w was greater than 0.5 m s^{-1}. Parameter σ is the fractional number of cloudy LES grid cells for each coarse-graining subdomain.

With the definition of the subgrid cloudiness fraction σ in mind, a coarse-graining subdomain was further divided into a cloudy and an environmental part, similar to Eqs. (1) and (2):

$$\overline{\varphi}^{x} = \varphi_x = \frac{1}{N_x}\sum \varphi_n, \tag{7}$$

$$\overline{\varphi'^{x}} = \frac{1}{N_x}\sum (\varphi - \varphi_x)_n. \tag{8}$$

Here, x can be "c" or "e," representing the cloudy and environmental parts, respectively, as defined previously. Using Eqs. (7) and (8), the averaged vertical velocity and thermal variables in clouds and the environment could be diagnosed, where $N_c + N_e = N$, representing the number of cloudy and environmental LES grid cells in each coarse-graining subdomain. Therefore, the eddy transport in clouds and the environment can also be written as

$$\overline{w'\varphi'}^{x} = \frac{1}{N_x}\sum (w - w_x)(\varphi - \varphi_x)_n. \tag{9}$$

Following Siebesma and Cuijpers (1995), the subgrid flux of h ($\overline{w'h'}$) in a subdomain where $\sigma > 0$ can also be written as

$$\overline{w'h'} = \sigma(1-\sigma)(w_c - w_e)(h_c - h_e) + \sigma\overline{w'h'}^{c} + (1-\sigma)\overline{w'h'}^{e}. \tag{10}$$

This equation is a general expression without any approximation. The first term on the right-hand side of this equation is the convective mass flux and describes the contribution due to an average organized cloud and associated environment. The second term is the eddy transport in cloud and describes the correlated fluctuation within the clouds, which was omitted by Siebesma et al. (2007) due to $\sigma \ll 1$ in the convective ABL. The third term is the remaining eddy transport in the environment, which describes the correlated fluctuation within the environment. In practical implementation, since the third term is accounted for by the parameterization of subgrid mixing in vertical direction, Eq. (10) reduces to the following form that is widely used as the definition of the mass flux in the parameterization of subgrid convection:

$$\overline{w'h'} \approx \sigma(1-\sigma)(w_c - w_e)(h_c - h_e). \tag{11}$$

In this study, Eq. (10) was used as the basis to examine the variability of the subgrid flux with coarse-graining box size by using the subgrid cloudiness fraction, diagnosing the budget of the subgrid flux, and analyzing the relative importance of the convective mass flux, the eddy transport within clouds, and the eddy transport in the environment in an idealized extratropical deep convection scenario.

3. Benchmark simulation

a. Evolution of storm structure

Because of the unidirectional shear profile, the simulated storm evolves to form a mirror-image "splitting" supercell structure (Fig. 2). The initial thermal in the experiment evolved into a convective storm with a maximum updraft stronger than 6 m s^{-1} at 1 km AGL. Similar to previous simulation studies of the same scenario (e.g., Toy 2013), there was a clear bias in the location of the developing right-flank updraft associated with the cyclonic rotation. The rainwater clearly lagged behind the updraft, while it was collocated with the downdraft. At 90 min, the storm developed and moved to the right, and the updraft dominated almost half of the domain. Because of the lack of Coriolis force and the straight wind shear, the spatial structure of the storm remained symmetric. At 150 min, the storm split into six separate storms (four strong ones and two weak ones) that occupied almost the whole domain. Because the convection expanded, most of the statistical results were sampled from 1.5 to 2.5 h with 15-min intervals, unless stated otherwise. The temporal evolution of the domain-average precipitation (Fig. 3) shows that the surface rainfall occurred at 30 min. After the initial 30-min spinup, the domain-average precipitation rapidly increased from zero to 7 mm by 150 min. In the initial sounding, the convective available potential energy (CAPE) was 2200 J kg^{-1}, the lifting condensation level (LCL) was about 1300 m AGL, and the level of free convection (LFC) was 1400 m AGL. Once precipitation occurred, CAPE decreased rapidly, indicating that the convection removed the instability. The LFC increased to 1700 m, which was unfavorable for the development of convection. The LCL was constant before 90 min and then decreased to 1250 m, which may have been caused by the evaporation of precipitation at low levels (see discussion in section 3c). Consistent with the precipitation distribution, the maximum vertical velocity reached its peak and then remained constant in a quasi-steady fashion for the next 120 min. The evolution of these convection-related indices was distinct from the evolution of those in tropical convection, which tended to approach equilibrium with the forcing associated with the processes other than convection after spinup (see, e.g., Yano and Plant 2012; Toy 2013; Bechtold et al. 2014). In this supercell case, the convection was initiated by a local thermal bubble and driven by the preexisting

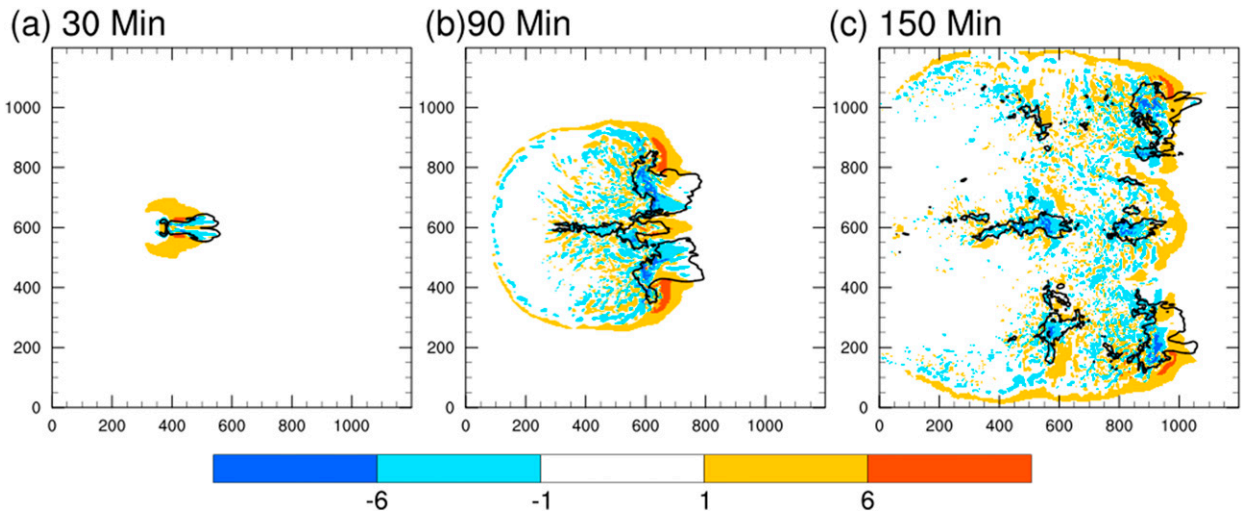

FIG. 2. Storm cell structure at (a) 30, (b) 90, and (c) 150 min. Vertical velocity (color shading) and rainwater mixing ratio (black contours of 1 g kg^{-1}) are shown at 1 km AGL.

CAPE. The convection eventually started dissipating after a few hours as the CAPE diminished.

b. Updraft and downdraft statistics

To demonstrate the similarities and differences in the structure of the supercell storm and tropical equilibrium convection, Fig. 4 shows the convective core statistics of vertical velocity, core diameter, and core mass flux for the updrafts and downdrafts from B100. These statistics were diagnosed at 15-min intervals for the last 1 h of the simulation. An updraft or a downdraft core is defined as having a vertical velocity magnitude of at least 1 m s^{-1} with a diameter of 500 m or more. The sampling method followed that of Khairoutdinov et al. (2009), and each plotted line represents the median (solid line) and 90th percentile (dashed line) value for the updraft (purple) and downdraft (blue) core properties. The strong updrafts (90th percentile) were much greater in magnitude in the midtroposphere (approximately 5 m s^{-1}) than in the strong downdraft (90th percentile; -3 m s^{-1}). The median core diameters changed little with height, which were less than 1 km everywhere for both the updraft and downdraft. The 90th percentile of the core diameters was 3 km from the cloud base to the midtroposphere and less in some locations. The mass flux in the median updraft and downdraft was similar insofar as the mass flux decreased slightly with height. The mass flux in the strong updrafts increased from the cloud base to 4 km, where the peak value was 9×10^3 kg m^{-1} s^{-1}. The peak mass flux in the downdrafts reached 7×10^3 kg m^{-1} s^{-1}, which was located at 1 km. These statistics show that strong updrafts have larger diameters and, therefore, larger mass fluxes. Conversely, strong downdrafts also have these features, which are very similar to those identified by Khairoutdinov et al. (2009). The median strength of the updraft and downdraft cores was in good agreement with GRPP Atlantic Tropical Experiment (GATE) observations (LeMone and Zipser 1980). For the 90th percentile of B100, the cloudy boxes had stronger updrafts and downdrafts, larger cores, and, therefore, more mass fluxes than those shown in the simulation by Khairoutdinov et al. (2009) that were consistent with observations in the tropics.

c. Sensitivity to grid spacing

Besides the LES run, horizontal resolution sensitivity experiments were also carried out to evaluate the performance of the model with a coarser horizontal grid spacing, such as 3 and 1 km, which are the typical resolutions of current regional operational NWP models, and to check the appropriate resolution to produce numerical convergence of the statistical properties shown in B100. Four other simulations with horizontal grid spacing of 200, 400, 1000, and 3000 m were performed (Table 1). The model configuration and initial sounding profile were kept the same as in the B100 run. The patterns of the hourly accumulated precipitation of the final hour of the runs were similar (Fig. 5), with a maximum domain-average accumulative precipitation greater than 25 mm within the hour. The horizontal distribution of precipitation bands was consistent with the storm structure shown in Fig. 2. All four strong storms were captured in the simulations with grid spacing of 1 km or finer, although the detailed structures of the intense precipitation were not identical due to the uncertainty of the model itself. For the other two weak storms behind, only the E200 run displayed some of the

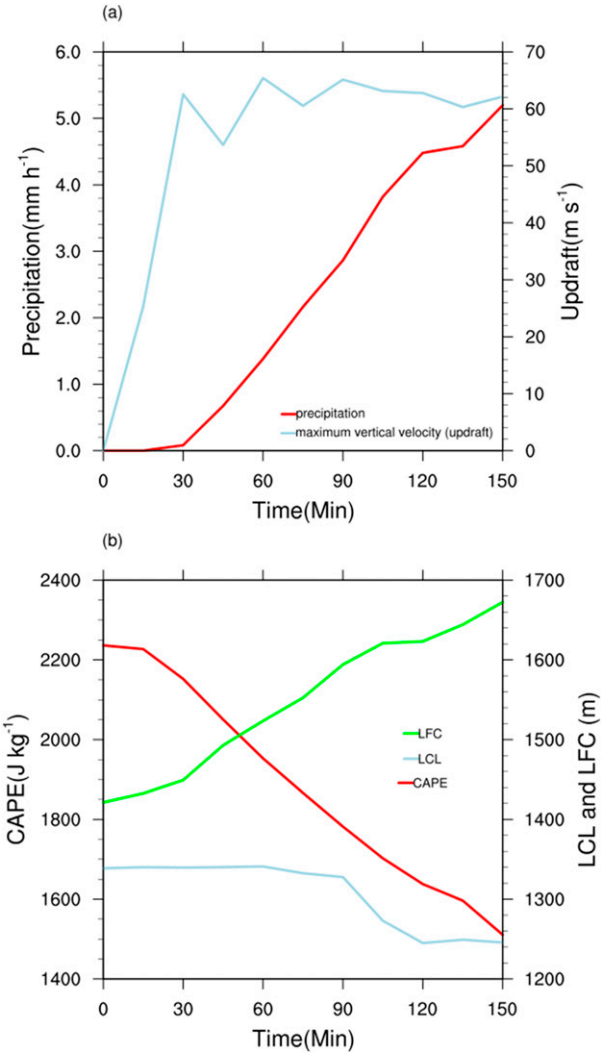

FIG. 3. Evolution of the (a) horizontally averaged precipitation and maximum vertical velocity, and (b) CAPE, LCL, and LFC.

features. However, the intensities of the precipitation in both experiments were weaker than in B100.

To further illustrate the characteristics of the associated cloud distribution, the horizontal distribution of cloud depth over the simulation domain at hour 2 of the different resolution runs was plotted (Fig. 6). This was used to visualize the clouds from shallow to deep convection that were associated with the convection system. For simplicity, the cloud depth was calculated using the height of the cloud top minus the cloud base, where the discontinuous vertical distribution of the cloud was ignored. Consistent with the precipitation pattern shown in Fig. 5, four deep cloud towers were captured by the model, except in E3000. Moving from B100 to the coarser resolution showed that the total amount of clouds tended to decrease, especially for the shallow, scattered clouds. With grid spacing of 1 km or finer, the pattern of deep clouds was very similar. For E3000, shallow clouds were rare, there were fewer deep clouds, and convection was more intense in some locations than for B100. Along the x direction, where the convection system moved eastward, the cloud depth exhibited a transition from cloud-free, scattered shallow clouds to collective deep clouds.

To compare precipitation in the convective cores and scattered convective edges, we performed conditional sampling by choosing a deep cloud domain ($60 < x < 120$ km and $70 < y < 120$ km) and a scattered shallow cloud domain ($0 < x < 60$ km and $0 < y < 50$ km; Fig. 6). Figure 7 shows the temporal evolution of the precipitation rate in the convection core area (domain A) and the less active convection area (domain B). Because the precipitation in domain B was weak, the units of the precipitation rate in domain B are 10^{-1} mm h^{-1}, whereas in domain A, they are mm h^{-1}. The precipitation rate in domain A increased rapidly before 120 min and then gradually increased in the last 30 min. The precipitation rate decreased with the reduction in grid spacing; however, the rates for B100 and E200 were similar. The precipitation rate of the 3-km run increased at a slower rate but was much stronger than the other higher-resolution runs, except 1 km at the end, which is similar to the findings of Weisman et al. (1997). There were two weak precipitation phases in domain B during the whole time. In the last 30 min, the precipitation in B100 developed earlier, but the intensity was similar to other experiments.

Figure 8 illustrates the vertical profiles of the horizontally averaged cloud (including cloud ice) hydrometeor concentration, the rain (including snow and graupel) hydrometeor concentration, and the cloud fraction over the last hour of the simulation for the different resolution runs. The model tended to produce more cloud and precipitating hydrometeors as the grid spacing became coarser (Figs. 8a,b), which was consistent with the variability of cloudiness (Fig. 8c). There were two vertical peaks of cloud hydrometeors, which were located at 1.5 and 6 km. The former was associated with scattered shallow cloud. The latter, and the peak of the precipitating hydrometeors at 9 km, were associated with deep cloud towers. Consistent with the profile of hydrometeors, the cloud fraction also exhibited a peak at a height of 1.5 km. Another peak of cloud fraction was located at 12 km, which was the anvil cloud with very low ice content. This anvil cloud at 12 km decreased as the grid spacing increased. Both the vertical cloud hydrometeor concentration and the cloudiness distribution exhibited a bimodal vertical distribution, which was associated with shallow cloud and deep cloud, respectively.

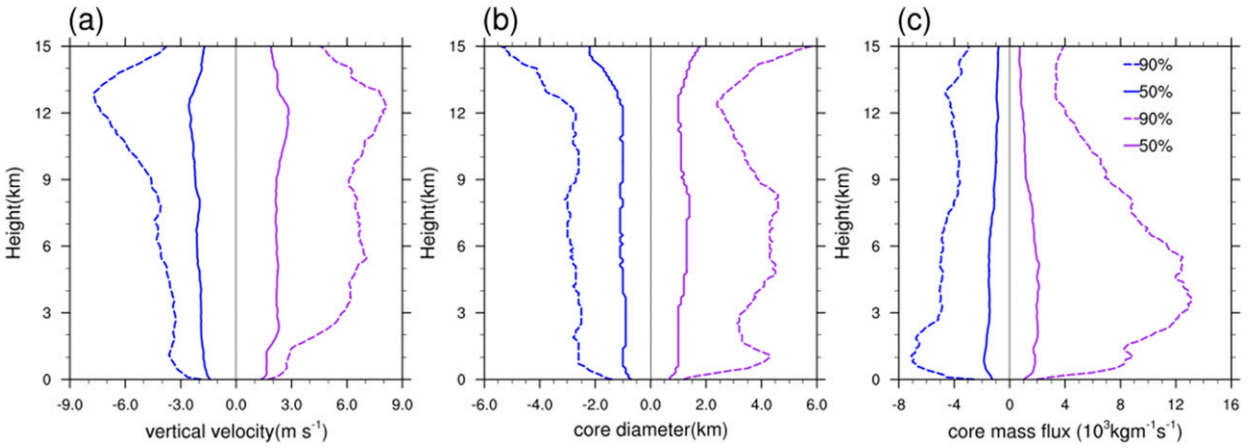

FIG. 4. Convective core statistics for the updraft (purple) and downdraft (blue) valid for last hour of the benchmark run. An updraft or a downdraft core is defined as having a vertical velocity magnitude of at least 1 m s^{-1} with a diameter of 500 m or more. The median (solid line) and 10th percentile (dashed line) are shown.

To quantify how subgrid physical properties of clouds varied as grid spacing changed, some flux terms essential to classical convective parameterization schemes, such as the mass flux, vertical flux of h, water vapor, and water hydrometeors (cloud and rain), were diagnosed. The mass flux was defined as $\rho\langle\overline{w}\rangle$, and the other three fluxes

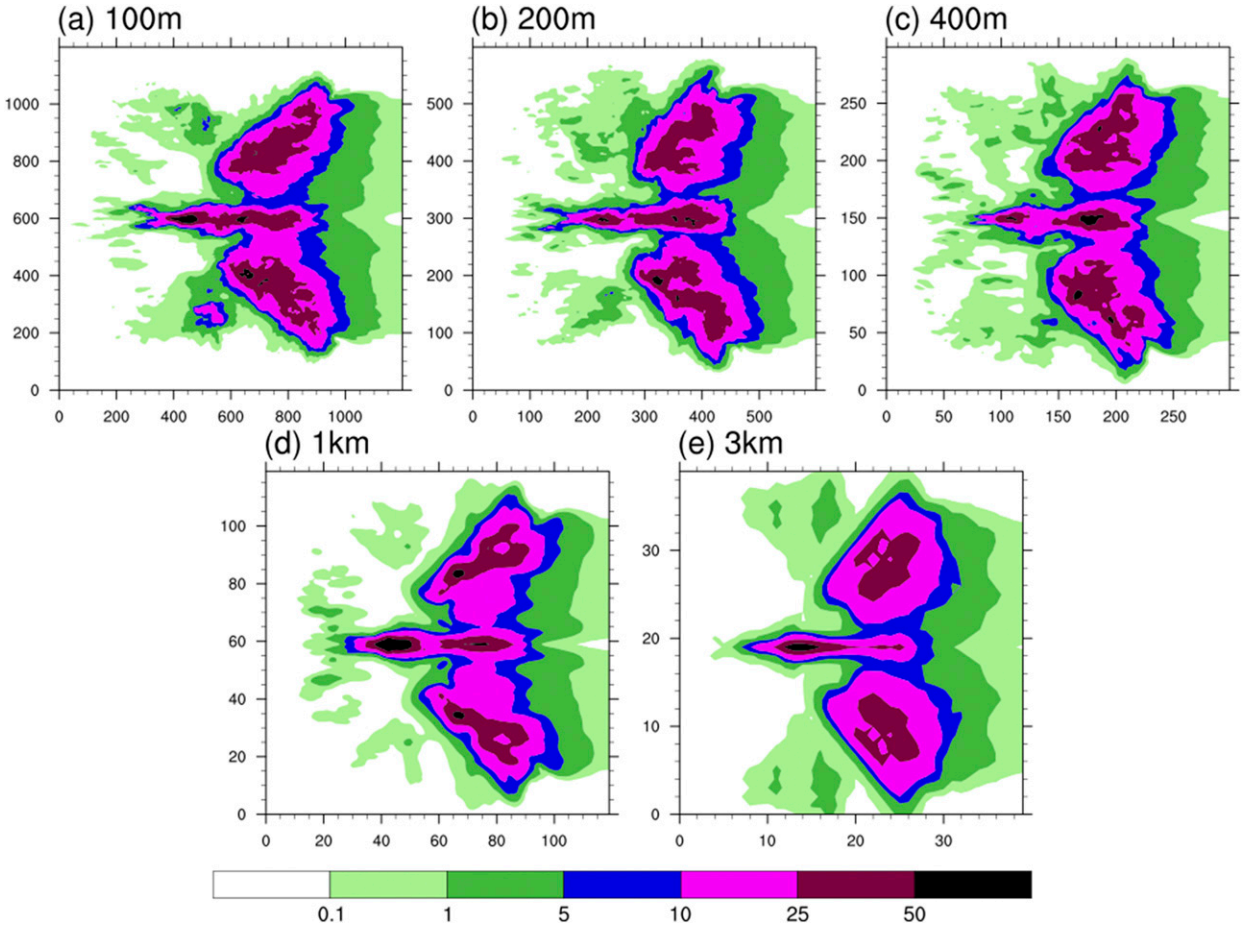

FIG. 5. Cumulative rainfall (mm) during the last hour (90–150 min) for runs with different horizontal grid spacing.

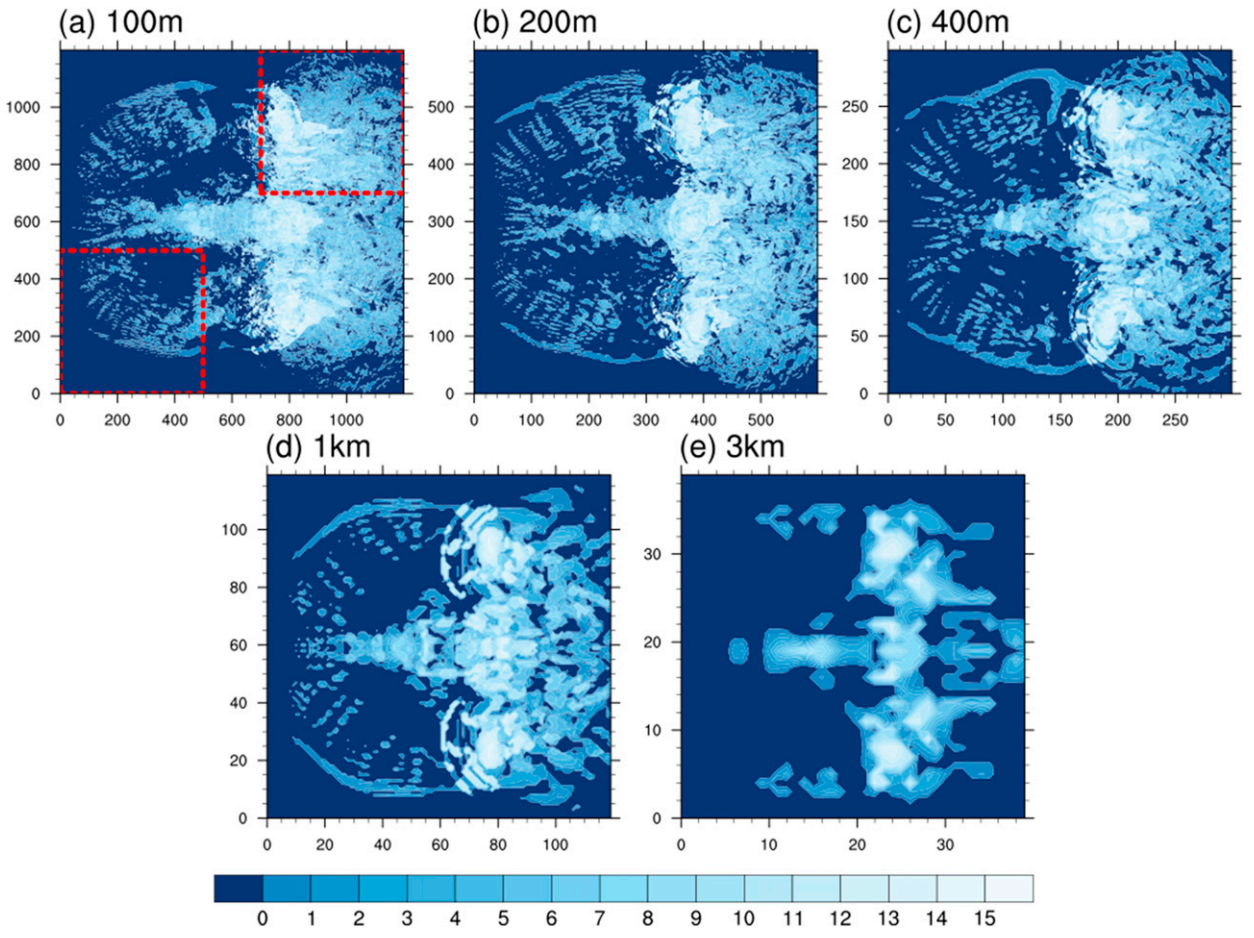

FIG. 6. Snapshot at hour 2 of the cloud depth from runs with resolutions of (a) 100 m, (b) 200 m, (c) 400 m, (d) 1 km, and (e) 3 km. Red boxes in (a) are areas for comparing the characteristics of convection. The top-right box ($60 < x < 120$ km and $70 < y < 120$ km) is defined as domain A, and the bottom-left box ($0 < x < 60$ km and $0 < y < 50$ km) is defined as domain B.

were calculated using Eq. (5), where $\overline{w\varphi}$ was obtained from each of the grid boxes of the different resolution runs. Figure 9 illustrates the domain-average vertical mass flux ($\rho\langle\overline{w}\rangle$), fluxes of h ($\rho\langle\overline{wh}\rangle$), water vapor ($\rho\langle\overline{wq_v}\rangle$), and water hydrometeors ($\rho\langle\overline{wq_l}\rangle$). The mass flux profiles (Fig. 9a) show the bulk vertical transport, which is mostly due to the deep convection, is well represented even on a grid spacing of 3 km, except an obviously excessive simulation with coarsening grid spacing. Dominated by mass flux, both the magnitude and shape of $\rho\langle\overline{wh}\rangle$ and $\rho\langle\overline{wq_v}\rangle$ (Figs. 9b,c) were simulated well, and at the same time, they tended to be overestimated in runs with coarser grid spacing. This tendency and overestimation were discussed by a few previous studies (e.g., Bryan et al. 2003; Roberts and Lean 2008).

It is worth noting that both E1000 and E3000 simulated too much $\rho\langle\overline{wq_l}\rangle$ above 4 km (Fig. 9d), which was a source of more precipitating hydrometeors and cloud fraction at upper levels. The negative flux of the hydrometeors below 2 km was mostly due to the precipitating hydrometeor flux in downdrafts, which was caused by the evaporation of precipitating hydrometeors. At this height, the fluxes were in a good agreement with each other for different resolution runs. This implies that the area average impact of the simulated downdrafts at 3-km grid spacing on the total vertical transport of moist static energy was much less sensitive to the grid spacing than the impact of the simulated updrafts. The resolved physical processes controlling downdrafts are sufficient in magnitude, but not at the right scale. For 3-km grid spacing, the hydrometeor flux was a little weak. It is important to note that the vertical hydrometeor flux associated with updrafts and downdrafts, as shown in Fig. 9d, is an intrinsic variable in the mass flux convective parameterization, and it is consistent with the definition of the total hydrometeor flux in the hydrometeor transport equation of the plume model

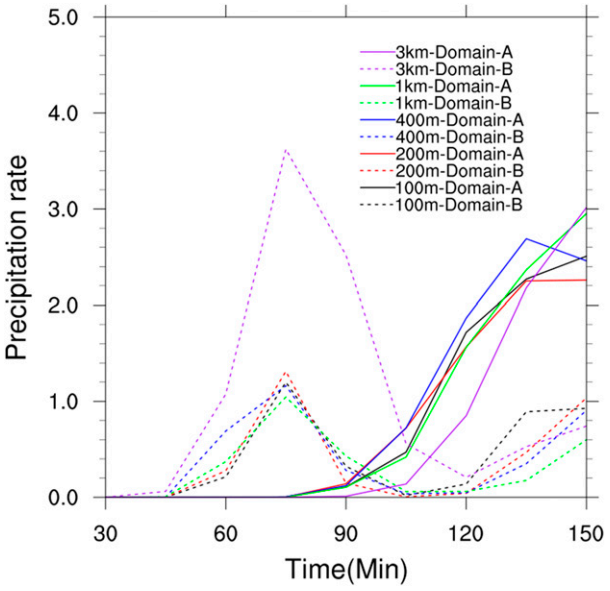

FIG. 7. Temporal evolution of the precipitation rate in domain A ($mm\,h^{-1}$) and B ($10^{-1}\,mm\,h^{-1}$) from runs with resolutions of 100 m, 200 m, 400 m, 1 km, and 3 km.

that is central to the mass flux parameterization. Although sedimentation is an integral part of actual vertical hydrometeor transport, it is not included in the flux shown in Fig. 9d because it is not accounted for in the mass flux convective parameterization.

Figure 10 shows the differences of $\rho\langle\overline{wh}\rangle$ between the four explicit runs and the 100-m benchmark run, pointing to some details of the deficiency of the total vertical transport flux of h in explicit runs, compared to the LES run. In the 1- and 3-km runs, the peaks of biases are at about 3 km, indicating these biases are associated with deep convection. In the 400-m run, there are two peaks in the bias. One is below 3 km, and the other is at about 4 km. In contrast to Fig. 9a, in which the peaks of the total vertical h flux for all the grid spacings are located above 3 km, this result indicates that the bias of the total h flux in the 400-m run is associated with the bias in the simulated shallower clouds. These imply that in the 400-m run, the subgrid effect due to deep convection is less important than that in the 1- and 3-km runs. Overall, the total flux of h was overestimated in all the explicit runs, except the 200-m run. This strongly suggests that at a grid spacing coarser than 200 m, it is necessary to account for the subgrid process for this idealized extratropical deep convection case in order to more accurately simulate the precipitation and cloud distributions.

Comparing Fig. 9 and Fig. 10 indicates that $\rho\langle\overline{w}\rangle$, $\rho\langle\overline{wh}\rangle$, $\rho\langle\overline{wq_v}\rangle$, and $\rho\langle\overline{wq_l}\rangle$ converged between B100 and E200. This is consistent with the finding of Khairoutdinov et al. (2009) that the statistical properties between their LES and a run converged at the 200-m grid spacing in the tropics. Our results also support the findings of Bryan et al. (2003) insofar as the 1-km grid spacing cannot reproduce the equivalent cloud structure, compared with the higher resolution, without subgrid cloud parameterization. Also, it should be pointed out that these overestimated fluxes of h result from a lack of subgrid fluxes.

It needs to be pointed out that the greatest assumption applied in this study is that the solution of the LES is the converged solution of the WRF Model for the idealized convection case. It should also be noted that explicit simulations at resolutions greater than that used in the LES, such as those investigated in this study, will inevitably produce errors at scales that are effectively resolved by the model grid. Since such errors are strongly dependent on the errors in physics parameterizations,

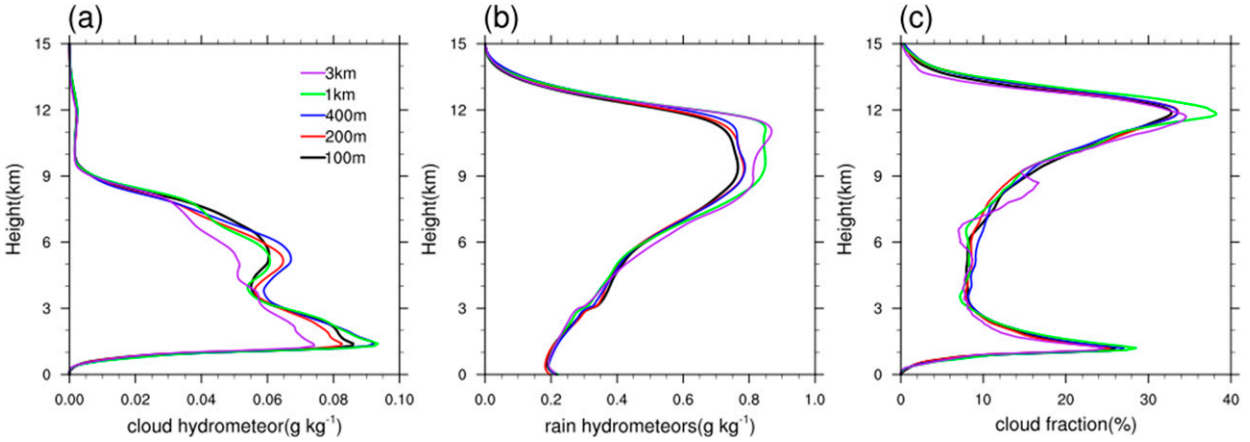

FIG. 8. (a) Vertical profiles of the horizontally averaged cloud hydrometeor concentration, (b) precipitating hydrometeor concentration, and (c) cloud fraction from runs with different horizontal resolutions.

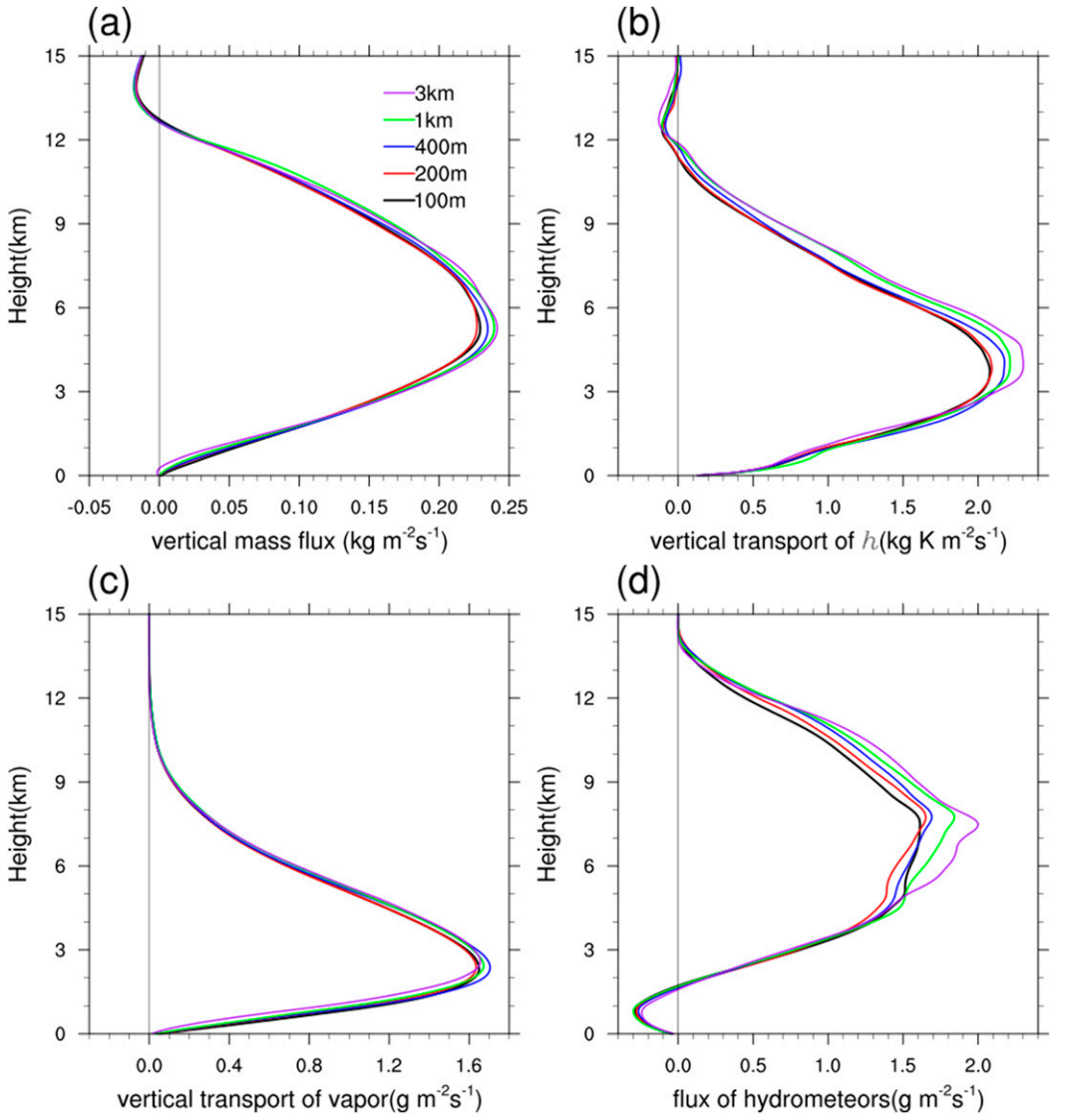

FIG. 9. As in Fig. 8, but for the (a) vertical mass flux, (b) vertical flux of moist static energy divided by c_p, (c) water vapor, and (d) hydrometeors.

particularly in the cloud microphysics parameterization (e.g., Kim et al. 2013; Potvin and Flora 2015), it is important to note that the diagnosed numerical aspects of the vertical distributions of grid-resolved and subgrid cloud properties shown in this study are expected to vary with the choice of microphysics and other physics (horizontal subgrid mixing in particular). For example, repeating the above experiments with the WSM6 microphysics scheme (Hong and Lim 2006), rather than the Thompson microphysics scheme, produced substantial changes in each horizontal resolutions. Figure 11 shows the patterns of cumulative precipitation with the WSM6 scheme are significantly different from that with the Thompson scheme during the last hour of the simulation. The area of cumulative precipitation greater than 10 mm in the run with the WSM6 scheme is greater than that with the Thompson scheme. In addition to the differences in the horizontal distribution of cumulative precipitation, there are small but noticeable differences in the variability associated with horizontal resolution change in the profiles of averaged vertical fluxes of mass, h, water vapor, and hydrometeors between the runs with the WSM6 and the Thompson schemes (Fig. 12 vs Fig. 9). These results indicate that if it is a valid assumption that the solution of the LES carried out in this study is the converged solution of the WRF Model for the idealized convection case, the convergence trend of the WRF Model is dependent on what physics configuration/choice

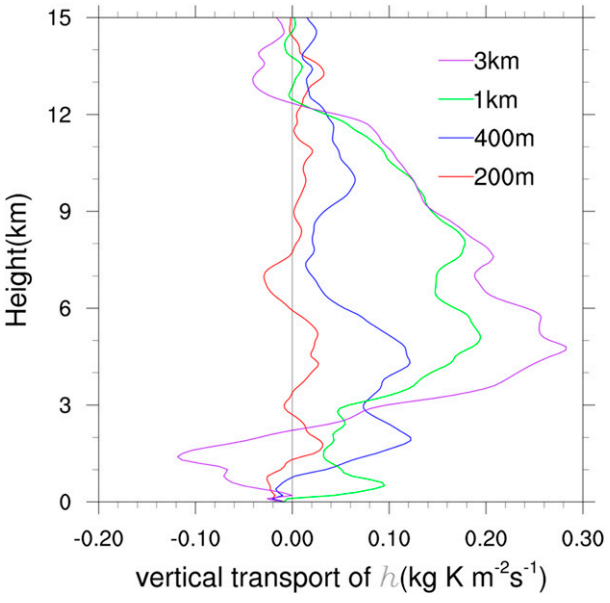

FIG. 10. Differences in the vertical transport of h divided by c_p between the explicit runs and B100.

is used for representing subgrid processes. They also show, consistent with the results from Kim et al. (2013) and Potvin and Flora (2015), that explicit simulations at resolutions greater than the LES will inevitably produce biases in the simulated storm structure and cloud properties, and the biases are dependent on the physics configuration/choice used for representing subgrid processes. This strongly suggests that any attempt to develop a parameterization of subgrid clouds at the resolutions used in this study (the so-called gray-zone resolutions) should account for the fact that what needs to be parameterized numerically on the subgrid scale is dependent on the specific choice of the microphysics scheme for the grid-resolved clouds.

Next, we examine how the subgrid fluxes would change with model grid spacing by coarse-gain analysis of the output form benchmark run.

4. Coarse-grain analysis of the output from the LES

a. Subgrid vertical transport profiles

Most subgrid cumulus convection schemes include the parameterization of the subgrid transport of related variables, which include mass, temperature, water vapor, and their feedbacks, by compensating subsidence and producing cloud and rain in the grid boxes. At the gray-zone scale, it is important to understand how parameterization of these subgrid processes should vary with change in grid spacing. Figure 13 shows the averaged LES coarse-graining vertical profiles of the horizontally averaged subgrid fluxes of h ($\rho\langle\overline{w'h'}\rangle$), water vapor ($\rho\langle\overline{w'q'_v}\rangle$), and water hydrometeors (all liquid and solid hydrometeors, $\rho\langle\overline{w'q'_l}\rangle$). Although the magnitude was much greater than that in Wu and Arakawa (2014), due to the different model resolution of the benchmark run, the vertical pattern of $\rho\langle\overline{w'h'}\rangle$ was very similar. Because h is conserved under moist adiabatic processes, it can be used to visualize the subgrid mass flux variability. Below 1 km, $\rho\langle\overline{w'h'}\rangle$ remained nearly constant in a well-mixed ABL that was consistent with the vertical velocity and h profiles. From 1 to 2 km, $\rho\langle\overline{w'h'}\rangle$ showed that entrainment dominated the subgrid cloud processes, and the prevailing detrainment gradually depleted the updraft mass flux from 2 to 15 km. The shape of $\rho\langle\overline{w'q'_v}\rangle$ was consistent with that of $\rho\langle\overline{w'h'}\rangle$. Because the total coarse-grained vertical transport of flux remains unchanged as the coarse-grained grid size varies, the fraction of subgrid flux to the total flux at different grid size can also be examined. In fact, the $\rho\langle\overline{w'h'}\rangle$ is about 40%, and the $\rho\langle\overline{w'q'_v}\rangle$ is about 16% to total flux for 3-km grid spacing at 3-km height. In general, these two subgrid flux variables decreased when the box size became finer. As a result, when the box sizes became very small, the unresolved fluxes gradually disappeared.

The production and sink of water hydrometeors in the subgrid cloud processes is also an important issue. Below 2.5 km, $\rho\langle\overline{w'q'_l}\rangle$ (Fig. 13c) for the 3-km box size was obviously negative, which was associated with the subgrid downdraft. It is found that for a box size finer than 3 km, this negative $\rho\langle\overline{w'q'_l}\rangle$ was reduced, which was consistent with the total hydrometeor flux of the explicit run. This suggests that there is not much that is associated with downdrafts on the subgrid scale below the cloud base that needs to be parameterized. From 2.5 to 5 km, the water hydrometeor flux increased. This was mostly due to the transport of the condensation of water vapor because detrainment was dominant at this level, as shown in Fig. 13a. Water hydrometeors were reduced by 70% from 4.5 to 12 km, and the remaining 30% was lost at the top of the cloud. This suggests that cloud and precipitating hydrometeor detrainment occurred both at the midlevel of the cloud and at the cloud top. Note that these trends are also seen in the tests using WSM6 microphysics; see Fig. 14.

b. Cloudiness fraction and its relationship with subgrid transport

Figure 15 shows the vertical distribution of $<\sigma>$ (average over the $\sigma > 0$ subdomains) with different coarse-graining box sizes from the coarse-graining data. Similar to Wu and Arakawa (2014), the vertical profiles of σ shown in this figure displayed a significant resolution and height dependence. Overall, σ increased as the box size decreased at all vertical elevations. Comparing the box size of 3 km with the shear case in Wu and Arakawa (2014), the maximum σ in this study was approximately

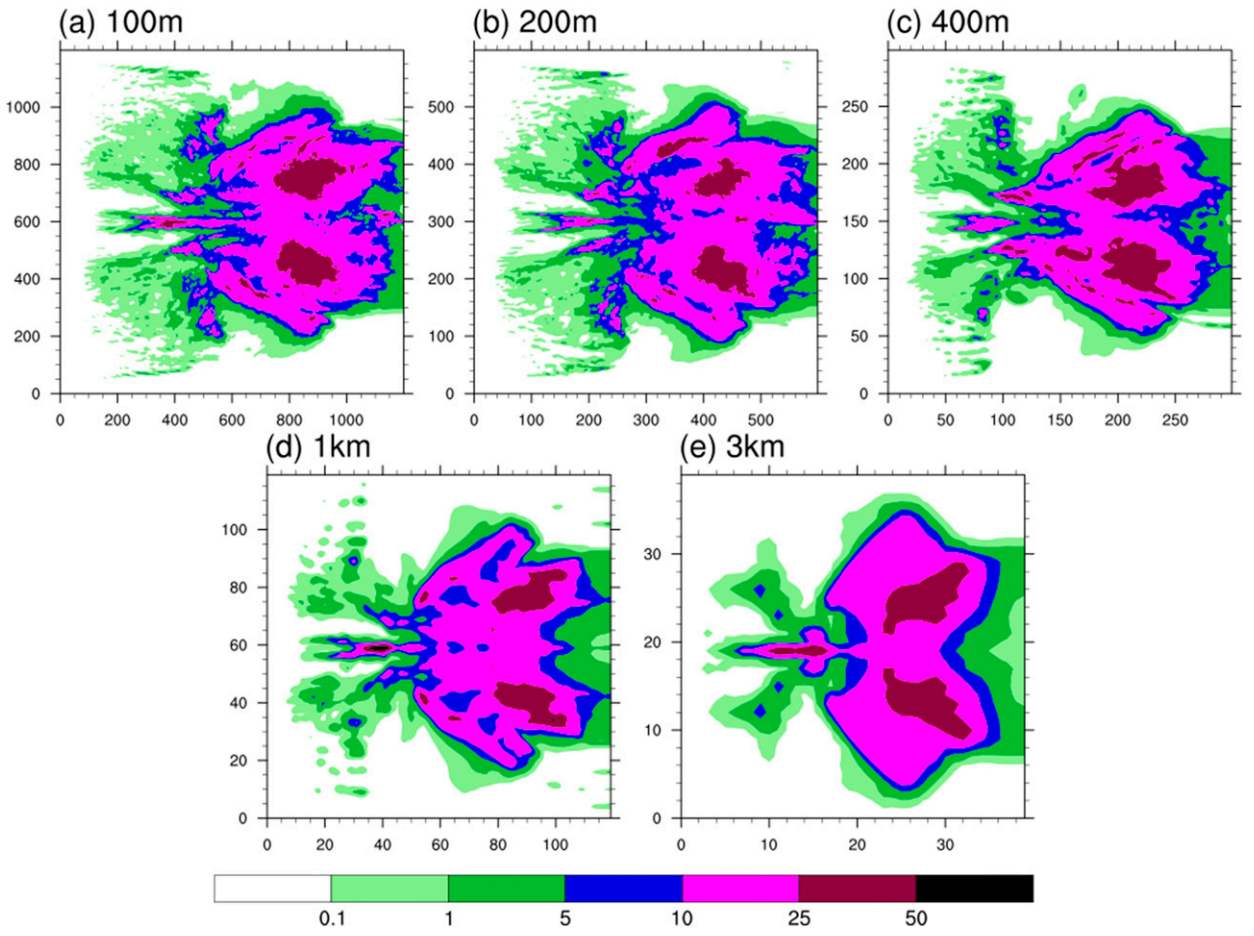

FIG. 11. As in Fig. 5, but for WSM6 microphysics.

0.35, while the maximum σ computed in Wu and Arakawa (2014) was nearly 0.8. This difference was mainly due to the different grid sizes used in respective high-resolution benchmark simulations, as well as the different scenarios of convection (i.e., the tropical vs extratropical convective system). In addition, the LES in this study resolved more detailed inhomogeneous cloud structures than the CRM used in Wu and Arakawa (2014). From 1 to 3 km in height, σ experienced a slight reduction due to the impact of shallow clouds. From 3 to 12 km, σ was approximately constant with height, which means that the vertical variability of σ can be omitted in deep clouds.

According to Eq. (10), $\rho\langle\overline{w'h'}\rangle$ can be decomposed into three terms: convective mass flux, eddy transport in clouds due to the multiple internal cloud structure, and eddy transport in the environment. The convective mass flux (Fig. 16a) was similar to $\rho\langle\overline{w'h'}\rangle$ below 10 km. Above 10 km, it became negative due to the negative buoyancy, which gradually decreased the vertical velocity in the cloud until it reached the cloud top. The profile of eddy transport in clouds (Fig. 16b) exhibited a typical deep cloud pattern with a magnitude that was as important as the convective mass flux term from 2.5 to 12 km. Below 2 km, the eddy transport in the environment was consistent with turbulent mixing in the convective ABL. The significant positive value above 12 km was associated with the anvil cloud in this layer. Compared with the other two terms, the eddy transport in the environment was small, which is consistent with the observations of LeMone and Pennell (1976). All three terms increased as the box size became coarser. Eddy transport in the environment was relatively much weaker than the other two terms, which is different from that in the ABL (Siebesma et al. 2007). The convective mass flux and the turbulence in cloud terms were comparable, which shows that the second term of Eq. (10) must be parameterized. The tests using WSM6 microphysics also exhibit similar trends (Fig. 17).

Figure 18 shows the first two terms in Eq. (10) in domain A, domain B, and the entire domain, with different box sizes at 2.5- and 5-km height. In domain A, with a 3-km box size, the convective mass flux term accounted for about 75% of $\rho\langle\overline{w'h'}\rangle$, while the eddy transport term

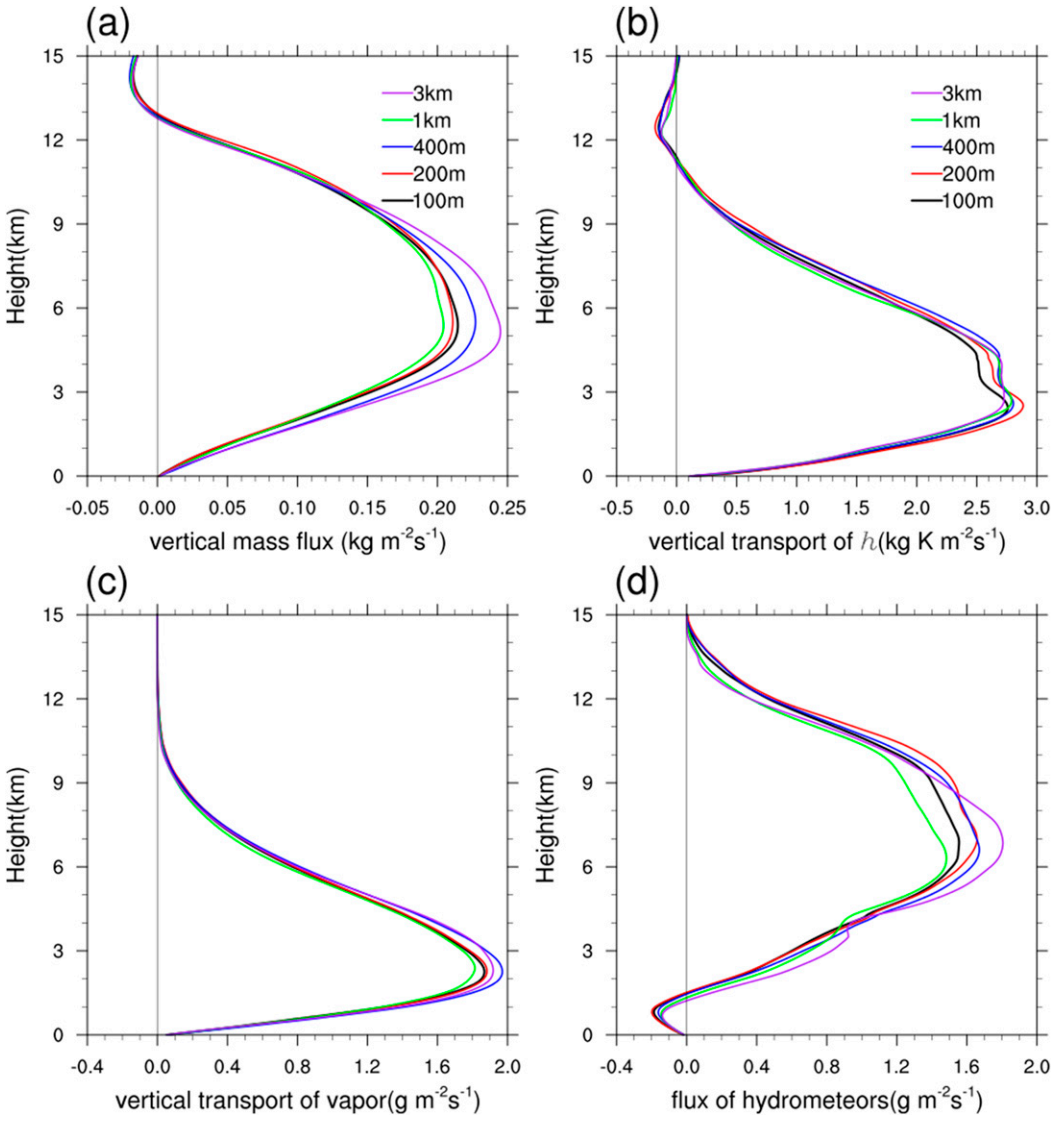

FIG. 12. As in Fig. 9, but for WSM6 microphysics.

in cloud accounted for 25%. The eddy transport in cloud became more important as the box size was reduced. At 5 km, because most samples in domain A were strong deep convection, the eddy transport in the cloud term was comparable with the convective mass flux term. When the box size was 400 m or finer, the eddy transport in the cloud was even larger than the convective mass flux term. In domain B, the contribution of the convective mass flux term to $\rho\langle\overline{w'h'}\rangle$ was dominant both at 2.5 and 5 km, where σ was significantly smaller and the convection was weak. In particular, despite the very small number of isolated deep updraft samples at 5-km height in domain B, the convective mass flux term was still large.

Zhu (2015) used an LES to diagnose the subgrid flux budget of six cloud cases. He found that Eq. (11) can account for most of the total fluxes for both shallow and deep convection, which is similar to the findings of Wang and Stevens (2000). However, in deep convection, a greater vertical velocity threshold for the updraft (e.g., $0.7\,\mathrm{m\,s^{-1}}$) was necessary. In the results shown here, the subgrid flux in the deep convection was determined by both convective mass flux and turbulence in the cloud. This occurred especially when the coarse-graining box size was finer than 1 km, where the magnitude of turbulence in the cloud term was larger than that of the convective mass flux term. When testing the criteria $w > 0.01\,\mathrm{m\,s^{-1}}$ and $w > 1.0\,\mathrm{m\,s^{-1}}$ combined with $q_c > 0.001\,\mathrm{g\,kg^{-1}}$, there was little change in the results (not shown). This suggests that in this case, the effect of turbulence in cloud should be accounted for. AW13 also found this significant difference between

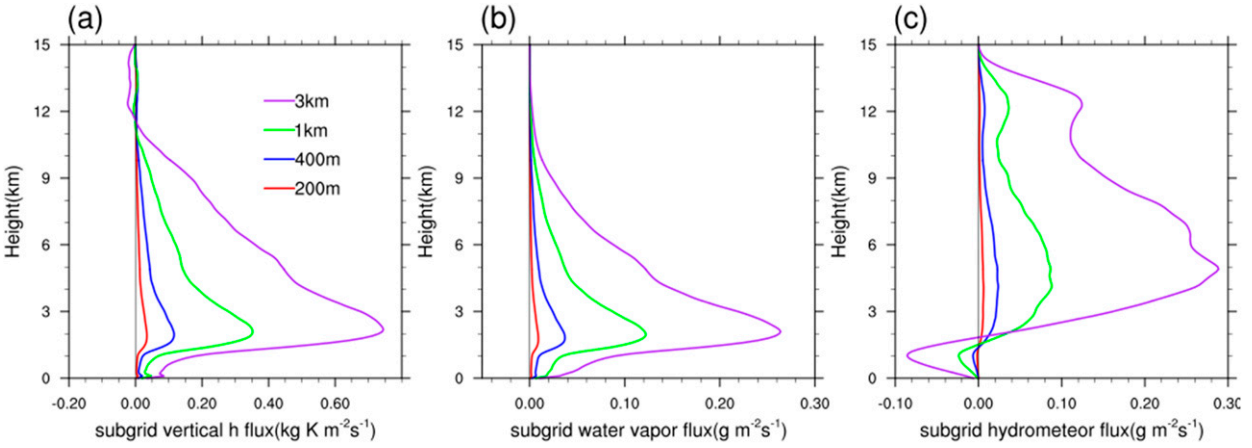

FIG. 13. (a) Averaged coarse-graining vertical profiles of the vertical transport of h divided by c_p, (b) water vapor, and (c) hydrometeors with grid sizes of 200 m, 400 m, 1 km, and 3 km.

the total subgrid flux of h and the convective mass flux when σ is large. They suggested that this difference is due to the multiple structures of the cloud itself and fitted the subgrid flux of h using the convective mass flux term with a triple w threshold (e.g., $0.5 \le w < 2\,\mathrm{m\,s^{-1}}$, $2 \le w < 4\,\mathrm{m\,s^{-1}}$, and $w \ge 4\,\mathrm{m\,s^{-1}}$).

As Eq. (11) shows, the convective mass flux term is determined by σ and the differences of w (h) between the cloud and the environment. If the difference of the w (h) terms is moved to the right-hand side of the equation, it becomes a nondimensional equation where the maximum value is located at $\sigma = 0.5$. When $\sigma = 1$ and $\sigma = 0$, the right-hand term becomes zero. Figure 19 shows the dependence on σ of the subgrid vertical transport of h using the same convective mass flux term as AW13. With box-size changes, the average peak magnitude of the convective mass flux term increased from $0.5\,\mathrm{kg\,K\,m^{-2}\,s^{-1}}$ (at 200-m box size) to $8\,\mathrm{kg\,K\,m^{-2}\,s^{-1}}$ (at 3-km box size). A strong relationship still existed between σ and the convective mass flux induced subgrid transport, which was consistent with that of AW13. This means that convective mass flux associated with deep convection is self-similar and can be parameterized by the hypothesis presented in AW13 at a much higher resolution. It is worth noting that in Fig. 19, there are noticeable gaps between the mean subgrid transport of h and the median value of all samples. These gaps become greater as the coarse-graining grid spacing increases. This suggests that the distribution of the coarse-grained subgrid updrafts is heavy tailed, particularly at the greater grid spacing, which is consistent with the Poisson distribution of subgrid updrafts that Plant and Craig (2008) proposed in a stochastic parameterization for deep convection.

5. Summary and discussion

This paper presents an LES of an idealized midlatitude supercell storm, which is different from deep tropical convection. The benchmark simulation used

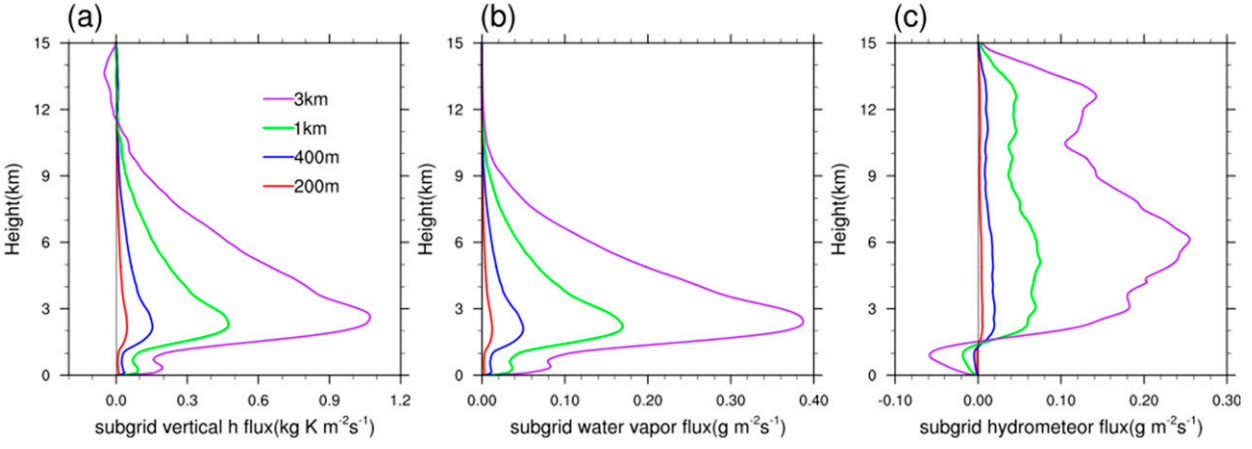

FIG. 14. As in Fig. 13, but for WSM6 microphysics.

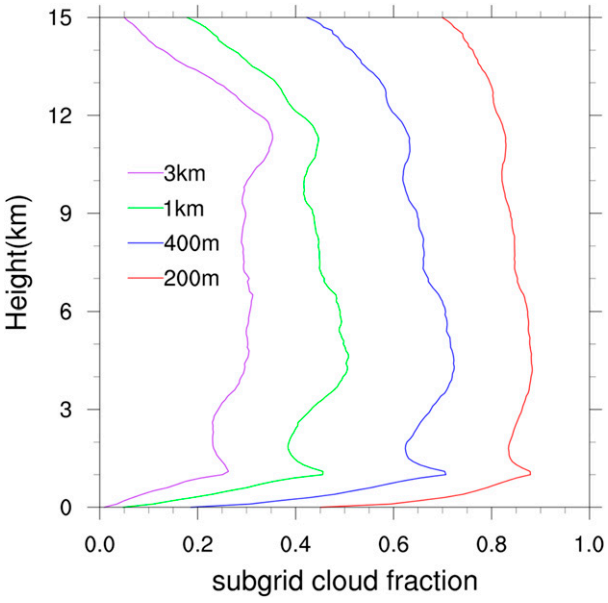

FIG. 15. As in Fig. 13, but for the subgrid cloudiness fraction.

$1200 \times 1200 \times 200$ grid points with horizontal and vertical grid spacing of 100 m. The convection system was initiated with a 3 K perturbation at the initial time and expanded over the whole domain in 150 min, which depicted a typical supercell storm evolution that compared well with previous studies. The domain-averaged accumulative precipitation increased due to the expansion of the rainfall area, and the maximum updraft became steady after 30 min. At the same time, the CAPE decreased and the LFC became higher, indicating that the instability reduced rapidly (Fig. 3). This suggests a nonequilibrium state of the convection process. The updraft and downdraft core statistics showed that the median of these characteristics was similar to that in the tropics, while the extreme values of the present case were much stronger for both updrafts and downdrafts (Fig. 4).

A series of sensitivity experiments using different horizontal resolutions was conducted with horizontal grid spacing of 200 m, 400 m, 1 km, and 3 km (Table 1), but with the same initial fields, model domain, vertical levels, time step, and physics configurations. These explicit runs were compared with the coarse-grained output of the LES run to evaluate the impact of unresolved processes on the simulation of the idealized case and the sensitivity of the impact to the horizontal resolution of the model. All the explicit runs, except for the 3-km run, reproduced the six splitting storms and the associated cloud horizontal distributions (Figs. 5, 6). The coarser-resolution runs tended to produce more precipitation induced by deep clouds but underestimated the precipitation and shallow convective clouds (Fig. 7). The horizontally average cloud properties (i.e., hydrometeor content and cloud fraction) showed a similar increasing tendency as the grid spacing increased (Fig. 8). The statistics of mass flux, the vertical transport of h, water vapor, cloud hydrometeors, and precipitating hydrometeors showed that there was numerical convergence only between the 200-m and LES runs (Figs. 9, 10). These results suggest that the 1-km grid spacing was capable of simulating the overall precipitation produced by the supercell deep convection. However, to resolve the cloud structure, the 200-m grid spacing was necessary. To achieve a better representation of cloud production and development in this case with a coarser grid spacing model, the effect of subgrid cloud variability should be considered.

The LES provides useful information on what aspects of cloud properties need to be parameterized on the

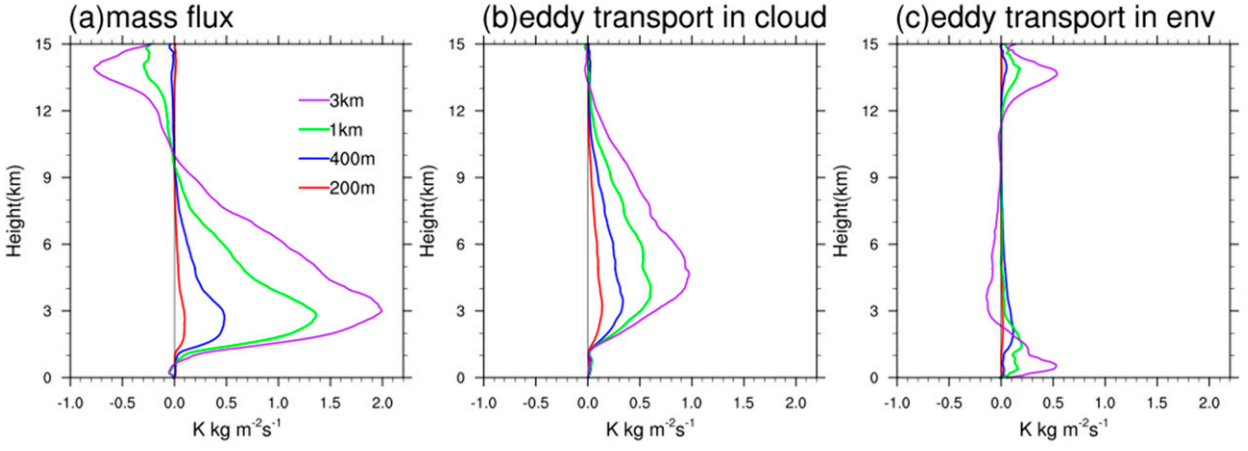

FIG. 16. As in Fig. 13, but for the (a) subgrid transport of h divided by c_p contributed by mass flux, (b) eddy transport in the environment, and (c) eddy transport in the updraft.

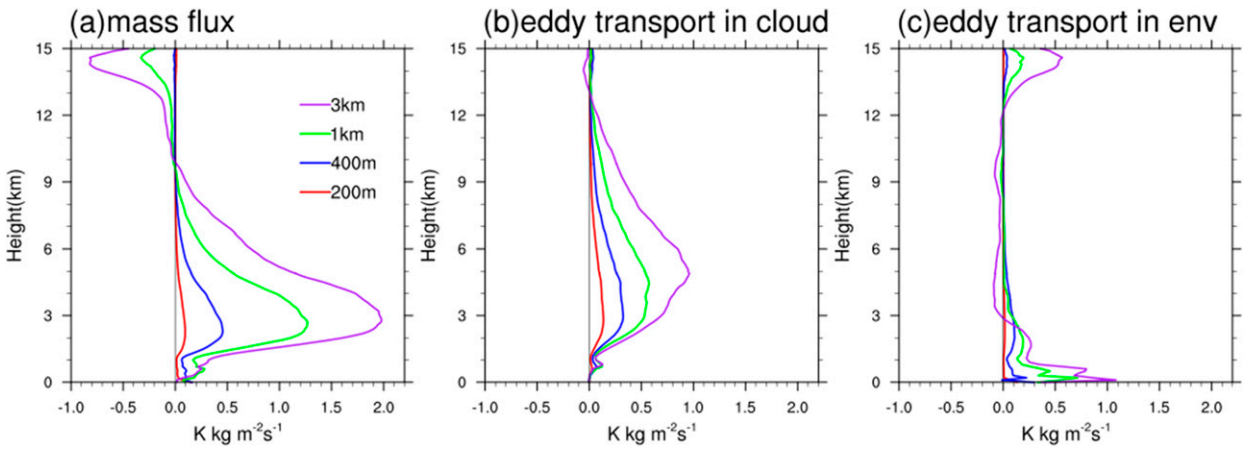

FIG. 17. As in Fig. 16, but for WSM6 microphysics.

subgrid scale if the mass flux parameterization is used. Using the coarse-graining approach, the vertical distribution and the resolution dependence of the subgrid vertical variability of h, water vapor, and water hydrometeors, which are the key processes of convection parameterization, were also analyzed. As expected, the subgrid flux of h and water vapor increased as the box size increased. The subgrid flux of water hydrometeors showed that the detrainment was nearly constant from 5 km to the cloud top (Fig. 13). Furthermore, the subgrid cloudiness fraction σ was introduced in the present work to evaluate the importance of the subgrid cloud process. The σ was resolution and convection system dependent (Fig. 15). The frequency of the σ distribution showed that 50% or more samples were resolvable with a grid size 400 m or finer, while more than 50% of the samples needed parameterization with a grid size of 3 km. The σ in the convective core area was much larger than that in the convectively less active area when the grid spacing was the same.

We also examined how the scale-awareness control parameter of the mass flux convection parameterization should change with the horizontal grid size if it is specified following AW13. The subgrid flux can be divided into three terms, where only the convective mass flux term is considered important in traditional convective parameterization. We found that the subgrid flux contributed by the mass flux term could not account for most of the flux (Fig. 16). The eddy transport term was comparable with the mass flux term, especially in the

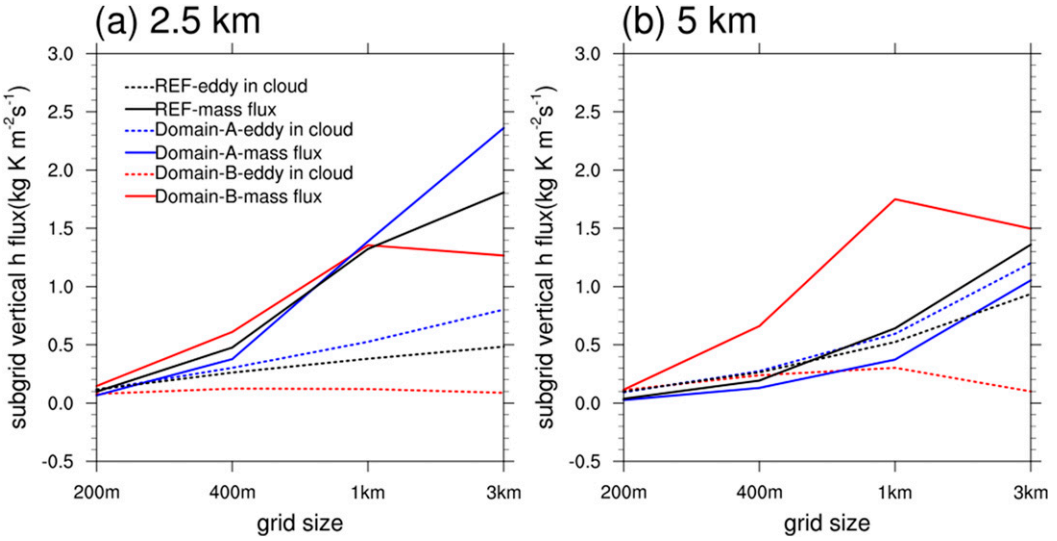

FIG. 18. Average subgrid flux of h divided by c_p (kg K m^{-2} s^{-1}) in domain A, domain B, and the whole domain at (a) 2.5 and (b) 5 km.

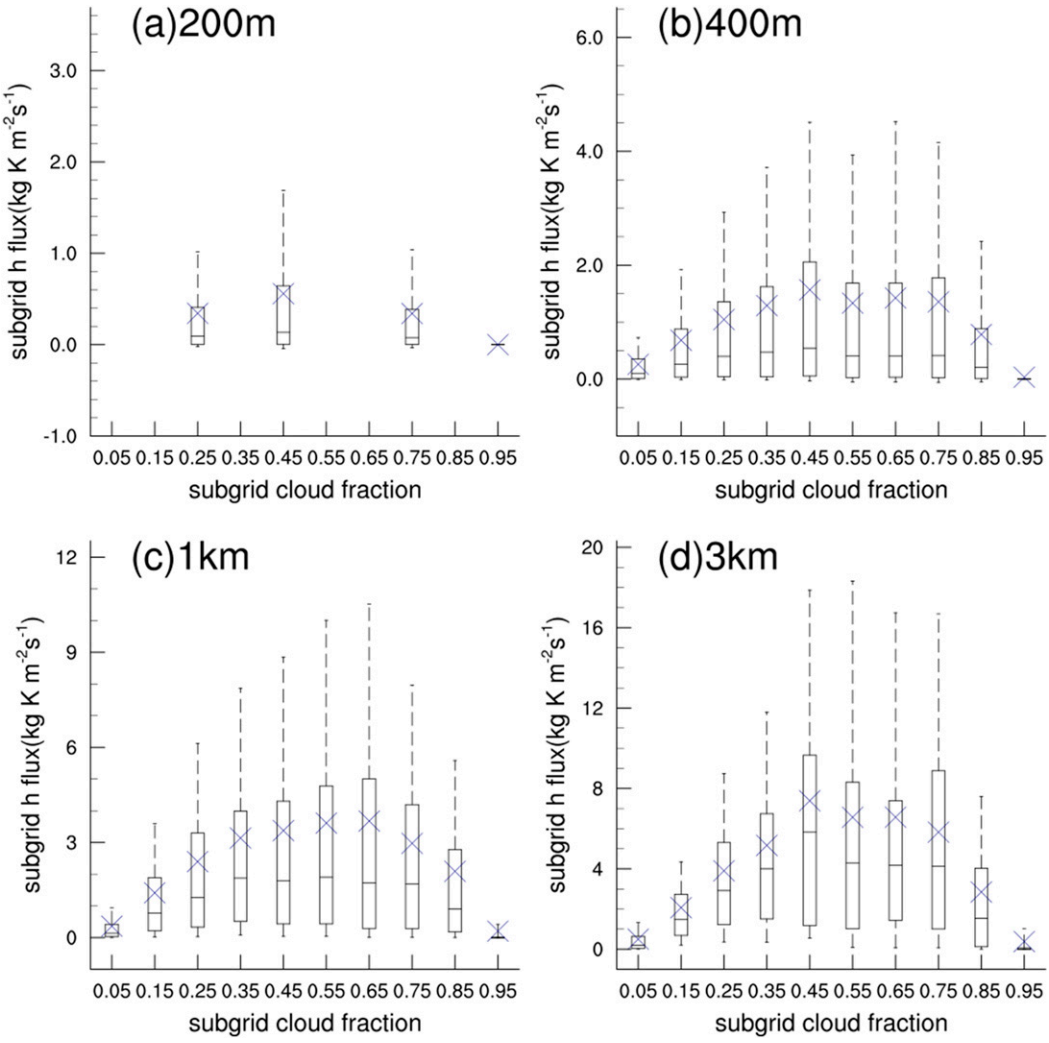

FIG. 19. The σ-dependence distribution of the subgrid transport of h divided by c_p, contributed by mass flux (kg K m^{-2} s^{-1}). The x axis is σ, and the crosses represent the average values. The boxplot extends from the 25th to the 75th percentile. The horizontal bars within the boxes denote the median values. The ends of the whiskers are drawn to the 10th- and 90th-percentile values. (a)–(d) 200 m, 400 m, 1 km, and 3 km LES coarse-graining data, respectively.

convective core area, where the eddy transport term in the cloud was more important than the convective mass flux term (Fig. 18). This implies that the eddy transport term should also be considered in scale-aware subgrid convective parameterization. This analysis also confirmed the quadratic parabolic relation between σ and subgrid transport at a higher resolution using a midlatitude storm case (Fig. 19).

The results from the comparison among Figs. 9, 10, and 11 show that the biases in the explicit simulations relative to the LES are not negligible. In particular, the absence of the subgrid transport flux of h in the explicit runs tends to result in a greater average vertical transport of h than the coarse-grained analysis of the LES indicates. This strongly suggests that excluding the use of a parameterization of the subgrid transport flux of h in the simulation at a gray-zone resolution is not prudent. Assuming that the output of the LES is a ''true'' solution, the above results provide useful information about what a parameterization of subgrid convection/clouds should accomplish in this case. The coarse-graining analysis of the LES shows that the total flux of h in a simulation at a given grid spacing greater than that used in the LES are made of the resolvable and the subgrid (i.e., unresolved) components, the latter of which can only be parameterized as a function of resolvable processes. A correct parameterization of the subgrid component should work in such a way that the two components can be realized in the simulation at any given

grid spacing when the parameterization is activated in the simulation. Coarse-graining analysis of LES results, such as those present above, can be used to provide guidance for developing and evaluating the parameterization. In addition, it should be kept in mind that for real-time forecasts of deep convection, there are many sources of model uncertainties (e.g., initial and boundary conditions and physics parameterizations). This study provides only an estimate of how the vertical distributions of cloud properties vary with various horizontal resolutions.

The results from the coarse-graining analysis of the LES results in this study can potentially provide useful information for stochastic physics parameterization at the gray-zone resolutions. As shown by Sakradzija et al. (2016), it may be necessary to include stochastic effects in the parameterization of subgrid clouds, particularly shallow convective clouds. AW13 advocated that a stochastic parameterization should be developed based on the information deduced under appropriate physical constraints. The results from this study confirm that at a given gray-zone grid spacing, the parameterized mean subgrid transport of h in the vertical direction that is based on the concept of ensemble mean may not be able to represent a proper collective effect of all samples, at least in terms of area fraction of subgrid updrafts. Therefore, the results from this study may be helpful to deal with the challenge in the stochastic parameterization of deep convection because they contain useful statistical information about the uncertainty in the subgrid-scale processes for a given grid spacing, in particular with respect to subgrid cloud development associated with the subgrid transport due to inhomogeneous internal structure of updrafts.

Although the analysis in this study was focused on the vertical transport of h, this does not mean that the subgrid vertical momentum transport was not important. How to parameterize the momentum flux induced by the convective process at the gray-zone scale is still a complex issue and requires further work. Furthermore, the subgrid flux was originally three-dimensional. When the model grid spacing was finer (e.g., less than 10 km), the horizontal subgrid transport became more important. For the convection process, these terms have a close link with the detrainment and entrainment processes. When these terms are partially resolved at higher resolutions, the parameterization of detrainment and entrainment should also be scale aware at this scale. This will be part of our future work to further understand the effect of subgrid cloud processes and what should be included in convective parameterization.

Acknowledgments. We thank Nathan Dahl and two anonymous reviewers for their careful review of our manuscript and their many insightful comments and suggestions. The first author, Wei Huang, is grateful to the Physical Sciences Division of the NOAA/Earth System Research Laboratory in Boulder, Colorado, for hosting his visit between December 2016 and February 2017, which was helpful to the completion of the manuscript. This work is supported by the National Key Research and Development Program of China (2016YFE0109700) and the Natural Science Foundation of China (Grants 41575101 and 41505087).

REFERENCES

Arakawa, A., and W. H. Schubert, 1974: Interaction of a cumulus cloud ensemble with the large-scale environment. Part I. *J. Atmos. Sci.*, **31**, 674–701, https://doi.org/10.1175/1520-0469(1974)031<0674:IOACCE>2.0.CO;2.

——, and C.-M. Wu, 2013: A unified representation of deep moist convection in numerical modeling of the atmosphere. Part I. *J. Atmos. Sci.*, **70**, 1977–1992, https://doi.org/10.1175/JAS-D-12-0330.1.

——, J.-H. Jung, and C.-M. Wu, 2011: Toward unification of the multiscale modeling of the atmosphere. *Atmos. Chem. Phys.*, **11**, 3731–3742, https://doi.org/10.5194/acp-11-3731-2011.

Bechtold, P., N. Semane, P. Lopez, J.-P. Chaboureau, A. Beljaars, and N. Bormann, 2014: Representing equilibrium and nonequilibrium convection in large-scale models. *J. Atmos. Sci.*, **71**, 734–753, https://doi.org/10.1175/JAS-D-13-0163.1.

Bryan, G. H., and R. Rotunno, 2005: Statistical convergence in simulated moist absolutely unstable layers. *11th Conf. on Mesoscale Processes*, Albuquerque, NM, Amer. Meteor. Soc., 1M.6, https://ams.confex.com/ams/32Rad11Meso/techprogram/paper_96719.htm.

——, J. C. Wyngaard, and J. M. Fritsch, 2003: Resolution requirements for the simulation of deep moist convection. *Mon. Wea. Rev.*, **131**, 2394–2416, https://doi.org/10.1175/1520-0493(2003)131<2394:RRFTSO>2.0.CO;2.

Ching, J., R. Rotunno, M. LeMone, A. Martilli, B. Kosovic, P. Jimenez, and J. Dudhia, 2014: Convectively induced secondary circulations in fine-grid mesoscale numerical weather prediction models. *Mon. Wea. Rev.*, **142**, 3284–3302, https://doi.org/10.1175/MWR-D-13-00318.1.

Dorrestijn, J., D. T. Crommelin, A. P. Siebesma, and H. J. Jonker, 2013: Stochastic parameterization of shallow cumulus convection estimated from high-resolution model data. *Theor. Comput. Fluid Dyn.*, **27**, 133–148, https://doi.org/10.1007/s00162-012-0281-y.

Gerard, L., 2007: An integrated package for subgrid convection, clouds and precipitation compatible with meso-gamma scales. *Quart. J. Roy. Meteor. Soc.*, **133**, 711–730, https://doi.org/10.1002/qj.58.

Hong, S.-Y., and J. O. J. Lim, 2006: The WRF Single-Moment 6-Class Microphysics Scheme (WSM6). *J. Korean Meteor. Soc.*, **42**, 129–151.

——, and J. Dudhia, 2012: Next-generation numerical weather prediction: Bridging parameterization, explicit clouds, and large eddies. *Bull. Amer. Meteor. Soc.*, **93**, ES6–ES9, https://doi.org/10.1175/2011BAMS3224.1.

Honnert, R., V. Masson, and F. Couvreux, 2011: A diagnostic for evaluating the representation of turbulence in atmospheric models at the kilometric scale. *J. Atmos. Sci.*, **68**, 3112–3131, https://doi.org/10.1175/JAS-D-11-061.1.

Khairoutdinov, M. F., and D. A. Randall, 2001: A cloud resolving model as a cloud parameterization in the NCAR Community

Climate System Model: Preliminary results. *Geophys. Res. Lett.*, **28**, 3617–3620, https://doi.org/10.1029/2001GL013552.

——, S. K. Krueger, C. H. Moeng, P. A. Bogenschutz, and D. A. Randall, 2009: Large-eddy simulation of maritime deep tropical convection. *J. Adv. Model. Earth Syst.*, **1**, 15, https://doi.org/10.3894/JAMES.2009.1.15.

Kim, J.-H., D.-B. Shin, and C. Kummerow, 2013: Impacts of a priori databases using six WRF microphysics schemes on passive microwave rainfall retrievals. *J. Atmos. Oceanic Technol.*, **30**, 2367–2381, https://doi.org/10.1175/JTECH-D-12-00261.1.

Klemp, J. B., and R. B. Wilhelmson, 1978: The simulation of three-dimensional convective storm dynamics. *J. Atmos. Sci.*, **35**, 1070–1096, https://doi.org/10.1175/1520-0469(1978)035<1070:TSOTDC>2.0.CO;2.

LeMone, M. A., and W. T. Pennell, 1976: The relationship of trade wind cumulus distribution to subcloud layer fluxes and structure. *Mon. Wea. Rev.*, **104**, 524–539, https://doi.org/10.1175/1520-0493(1976)104<0524:TROTWC>2.0.CO;2.

——, and E. J. Zipser, 1980: Cumulonimbus vertical velocity events in GATE. Part I: Diameter, intensity and mass flux. *J. Atmos. Sci.*, **37**, 2444–2457, https://doi.org/10.1175/1520-0469(1980)037<2444:CVVEIG>2.0.CO;2.

——, F. Chen, M. Tewari, J. Dudhia, B. Geerts, Q. Miao, R. L. Coulter, and R. L. Grossman, 2010: Simulating the IHOP_2002 fair-weather CBL with the WRF-ARW–Noah modeling system. Part II: Structures from a few kilometers to 100 km across. *Mon. Wea. Rev.*, **138**, 745–764, https://doi.org/10.1175/2009MWR3004.1.

McGee, C. J., and S. C. van den Heever, 2014: Latent heating and mixing due to entrainment in tropical deep convection. *J. Atmos. Sci.*, **71**, 816–832, https://doi.org/10.1175/JAS-D-13-0140.1.

Plant, R., and G. C. Craig, 2008: A stochastic parameterization for deep convection based on equilibrium statistics. *J. Atmos. Sci.*, **65**, 87–105, https://doi.org/10.1175/2007JAS2263.1.

Potvin, C., and M. Flora, 2015: Sensitivity of idealized supercell simulations to horizontal grid spacing: Implications for warn-on-forecast. *Mon. Wea. Rev.*, **143**, 2998–3024, https://doi.org/10.1175/MWR-D-14-00416.1.

Randall, D., M. Khairoutdinov, A. Arakawa, and W. Grabowski, 2003: Breaking the cloud parameterization deadlock. *Bull. Amer. Meteor. Soc.*, **84**, 1547–1564, https://doi.org/10.1175/BAMS-84-11-1547.

Roberts, N. M., and H. W. Lean, 2008: Scale-selective verification of rainfall accumulations from high-resolution forecasts of convective events. *Mon. Wea. Rev.*, **136**, 78–97, https://doi.org/10.1175/2007MWR2123.1.

Sakradzija, M., A. Seifert, and T. Heus, 2015: Fluctuations in a quasi-stationary shallow cumulus cloud ensemble. *Nonlinear Processes Geophys.*, **22**, 65–85, https://doi.org/10.5194/npg-22-65-2015.

——, ——, and A. Dipankar, 2016: A stochastic scale-aware parameterization of shallow cumulus convection across the convective gray zone. *J. Adv. Model. Earth Syst.*, **8**, 786–812, https://doi.org/10.1002/2016MS000634.

Shin, H. H., and S.-Y. Hong, 2013: Analysis of resolved and parameterized vertical transports in convective boundary layers at gray-zone resolutions. *J. Atmos. Sci.*, **70**, 3248–3261, https://doi.org/10.1175/JAS-D-12-0290.1.

Siebesma, A. P., and J. Cuijpers, 1995: Evaluation of parametric assumptions for shallow cumulus convection. *J. Atmos. Sci.*, **52**, 650–666, https://doi.org/10.1175/1520-0469(1995)052<0650:EOPAFS>2.0.CO;2.

——, and Coauthors, 2003: A large eddy simulation intercomparison study of shallow cumulus convection. *J. Atmos. Sci.*, **60**, 1201–1219, https://doi.org/10.1175/1520-0469(2003)60<1201:ALESIS>2.0.CO;2.

——, P. M. M. Soares, and J. Teixeira, 2007: A combined eddy-diffusivity mass-flux approach for the convective boundary layer. *J. Atmos. Sci.*, **64**, 1230–1248, https://doi.org/10.1175/JAS3888.1.

Skamarock, W. C., and J. B. Klemp, 2008: A time-split nonhydrostatic atmospheric model for weather research and forecasting applications. *J. Comput. Phys.*, **227**, 3465–3485, https://doi.org/10.1016/j.jcp.2007.01.037.

Thompson, G., R. M. Rasmussen, and K. Manning, 2004: Explicit forecasts of winter precipitation using an improved bulk microphysics scheme. Part I: Description and sensitivity analysis. *Mon. Wea. Rev.*, **132**, 519–542, https://doi.org/10.1175/1520-0493(2004)132<0519:EFOWPU>2.0.CO;2.

——, P. R. Field, R. M. Rasmussen, and W. D. Hall, 2008: Explicit forecasts of winter precipitation using an improved bulk microphysics scheme. Part II: Implementation of a new snow parameterization. *Mon. Wea. Rev.*, **136**, 5095–5115, https://doi.org/10.1175/2008MWR2387.1.

Toy, M. D., 2013: A supercell storm simulation using a nonhydrostatic cloud-resolving model based on a hybrid isentropic-sigma vertical coordinate. *Mon. Wea. Rev.*, **141**, 1204–1215, https://doi.org/10.1175/MWR-D-12-00215.1.

Wang, S., and B. Stevens, 2000: Top-hat representation of turbulence statistics in cloud-topped boundary layers: A large eddy simulation study. *J. Atmos. Sci.*, **57**, 423–441, https://doi.org/10.1175/1520-0469(2000)057<0423:THROTS>2.0.CO;2.

Weisman, M. L., and J. B. Klemp, 1982: The dependence of numerically simulated convective storms on vertical wind shear and buoyancy. *Mon. Wea. Rev.*, **110**, 504–520, https://doi.org/10.1175/1520-0493(1982)110<0504:TDONSC>2.0.CO;2.

——, and R. Rotunno, 2000: The use of vertical wind shear versus helicity in interpreting supercell dynamics. *J. Atmos. Sci.*, **57**, 1452–1472, https://doi.org/10.1175/1520-0469(2000)057<1452:TUOVWS>2.0.CO;2.

——, W. C. Skamarock, and J. B. Klemp, 1997: The resolution dependence of explicitly modeled convective systems. *Mon. Wea. Rev.*, **125**, 527–548, https://doi.org/10.1175/1520-0493(1997)125<0527:TRDOEM>2.0.CO;2.

——, C. Davis, W. Wang, K. W. Manning, and J. B. Klemp, 2008: Experiences with 0–36-h explicit convective forecasts with the WRF-ARW model. *Wea. Forecasting*, **23**, 407–437, https://doi.org/10.1175/2007WAF2007005.1.

Wu, C.-M., and A. Arakawa, 2014: A unified representation of deep moist convection in numerical modeling of the atmosphere. Part II. *J. Atmos. Sci.*, **71**, 2089–2103, https://doi.org/10.1175/JAS-D-13-0382.1.

Yano, J. I., and R. Plant, 2012: Finite departure from convective quasi-equilibrium: Periodic cycle and discharge–recharge mechanism. *Quart. J. Roy. Meteor. Soc.*, **138**, 626–637, https://doi.org/10.1002/qj.957.

——, J. L. Redelsperger, P. Bechtold, and F. Guichard, 2005: Mode decomposition as a methodology for developing convective-scale representations in global models. *Quart. J. Roy. Meteor. Soc.*, **131**, 2313–2336, https://doi.org/10.1256/qj.04.44.

Zhou, B., J. S. Simon, and F. K. Chow, 2014: The convective boundary layer in the terra incognita. *J. Atmos. Sci.*, **71**, 2545–2563, https://doi.org/10.1175/JAS-D-13-0356.1.

Zhu, P., 2015: On the mass-flux representation of vertical transport in moist convection. *J. Atmos. Sci.*, **72**, 4445–4468, https://doi.org/10.1175/JAS-D-14-0332.1.